Journal of Power Sources 195 (2010) 7140–7145

Contents lists available at ScienceDirect

Journal of Power Sources

journal homepage: www.elsevier.com/locate/jpowsour

# Effect of nickel–phosphorus interactions on structural integrity of anode-supported solid oxide fuel cells

Wenning Liu, Xin Sun*, Larry R. Pederson, Olga A. Marina, Moe A. Khaleel

*Pacific Northwest National Laboratory, Richland, WA 99352, United States*

ARTICLE INFO

*Article history:*
Received 21 April 2010
Received in revised form 1 June 2010
Accepted 2 June 2010
Available online 9 June 2010

*Keywords:*
Ni–YSZ anode degradation
SOFC structural integrity
Coal gas impurity
Phosphorus–nickel interaction
Mechanical properties

ABSTRACT

An integrated experimental/modeling approach was utilized to assess the structural integrity of Ni–yttria-stabilized zirconia (YSZ) porous anode supports during the solid oxide fuel cell (SOFC) operation on coal gas containing trace amounts of phosphorus impurities. Phosphorus was chosen as a typical impurity exhibiting strong interactions with the nickel followed by second phase formation. Tests were performed using Ni–YSZ anode-supported button cells exposed to 0.5–10 ppm of phosphine in synthetic coal gas at 700–800 °C. The extent of Ni–P interactions was determined by a post-test scanning electron microscopy (SEM) analysis. Severe damage to the anode support due to nickel phosphide phase formation and extensive crystal coalescence was revealed, resulting in electric percolation loss. The subsequent finite element stress analyses were conducted using the actual anode support microstructures to assist in degradation mechanism explanation. Volume expansion induced by the Ni phase alteration was found to produce high stress levels such that local failure of the Ni–YSZ anode became possible under the operating conditions.


## 1. Introduction

Solid oxide fuel cells (SOFCs) continue to show great promise as a future power source, with potential applications in both stationary and mobile power generation units [1]. With coal being the single largest domestic fuel source for the foreseeable future, the integration of coal gasification with SOFCs can potentially be a viable and efficient technology for clean power generation in the U.S. Among various SOFC designs, anode-supported planar cells seem to provide the best performance at the reasonable cost [2] and porous Ni–yttria-stabilized zirconia (YSZ) cermet is the anode of choice. Nickel, however, is highly susceptible to poisoning by multiple impurities, minor and trace elements, e.g., S, P, Se, As, Sb, that are naturally present in coals. These impurities exit in the fuel stream even after a sophisticated clean-up process [3–5]. Trembly et al. [6] performed an extensive thermodynamic analysis to identify the impurities that would potentially affect the performance of Ni–YSZ anodes. Cayan et al. presented a literature review [7] on the Ni–YSZ poisoning by different impurities.

It is widely recognized that different impurities cause different anode responses and lead to different degradation modes. The nickel–impurity interactions could be divided into two groups: surface interactions and bulk interactions. Sulfur, selenium, and chlorine impurities when present at reasonable low levels assuming initial coal gas clean-up are known to rapidly chemisorb on the Ni surface, form an adsorption layer and effectively block the active sites, resulting in a decreased anode activity for fuel oxidation [8]. SOFC performance loss is usually observed within a short period of time (1–30 h) followed by a new less active steady-state. The impurities desorb when no longer added to the feed gas, and the anode performance recovers to the initial or close to the initial level. No secondary Ni–S, Ni–Se, Ni–Cl phases were found or predicted for the realistic impurity concentration. Arsenic, phosphorus and antimony, on the other hand, readily react with the Ni under the SOFC operating conditions forming a series of intermetallic compounds: nickel arsenides, nickel phosphides, or nickel antimonides. The new phase formation starts near the fuel inlet indicating strong Ni–P, Ni–As or Ni–Sb interactions, and, depending on the test duration and impurity concentration, spreads further away from the inlet and deeper inside the anode support toward the active anode. A sharp boundary between converted and unconverted portions of the anode has been well documented [8–10]. Nickel depletion zones were formed during prolong exposures to P, As and Sb followed by abrupt and irreversible SOFC failures because of the electronic percolation loss. The cell degradation, however, started well before the active anode was converted, and was attributed to extensive coalesce of secondary phases into large grains that affected electrical connectivity through the anode support. Contributions of P and Sb adsorption layers to the anode degradation were much lesser, and no As adsorption layer was observed using analytical surface techniques [9,10].

While the electrochemical degradation of an SOFC anode in the presence of coal gas contaminants continues receiving a good deal of attention [6–11], impact of impurities on mechanical proper-

* Corresponding author. Tel.: +1 509 372 6489.
*E-mail address:* xin.sun@pnl.gov (X. Sun).

0378-7753/$ – see front matter © 2010 Elsevier B.V. All rights reserved.
doi:10.1016/j.jpowsour.2010.06.015

ties and structural integrity of the SOFC has not been studied as extensively yet. In anode-supported cells, the 0.3–0.9 mm porous Ni–YSZ provides the main structural support for the thin, 7–10 μm, YSZ electrolyte layer which is inherently susceptible to mechanical failures when subjected to moderate stresses [12,13]. When nickel is converted to the secondary phases, this process is accompanied by a considerable volume expansion, leading to localized stress concentrations. Such stress may be high enough to result in initiation and propagation of local cracks and severely compromise the structural integrity of the anode and the SOFC.

In this paper, the effect of the phosphorus impurity in coal-derived syngas on the mechanical degradation of Ni–YSZ anode was evaluated utilizing an integrated experimental/modeling approach. Post-exposure characterization of the Ni–YSZ was performed by scanning electron microscopy (SEM) and electron backscatter diffraction (EBSD). Based on the analyses performed, a subsequent finite element model was constructed. Stresses in the Ni–YSZ support upon Ni conversion to different Ni–P phases, $Ni_3P$, $Ni_5P_2$, $Ni_{12}P_5$, and $Ni_2P$, were investigated. The local volume change was described using the Pilling and Bedworth Ratio (PBR) [14–16]. Phase alteration was found to induce significant volume changes and result in high localized stress level in the contaminated region of the anode, such that the localized failure of the Ni–YSZ anode became possible. As time progresses, the propagation of the local failure can lead to the global failure of the anode support structure under the SOFC operating conditions. On the other hand, the high stress induced by the Ni phase conversion is localized within the contaminated region, and will not propagate outside the contaminated region.

## 2. Experimental

### 2.1. Anode composition and testing

Ni–YSZ anode-supported button cells were fabricated and tested as described previously [10]. The anode support was comprised of a Ni/YSZ bulk layer with a 40/60 vol.% solids ratio and approximately 30 vol.% porosity, and was approximately 0.9 mm in thickness. The active anode was approximately 5 μm in thickness and consisted of Ni/YSZ in a 50/50 vol.% solids ratio and 3 vol.% porosity. The electrolyte was 8 mol% YSZ (8 mol% yttria-stabilized zirconia), approximately 9 μm in thickness. Tests were performed in the synthetic coal gas, $H_2$–CO–$CO_2$–$H_2O$ = 30–23–21–26%, at 700–800 °C for 400–1700 h. Phosphorus at a concentration of 0.5–10 ppm was introduced as phosphine. Details of the experimental setup and electrochemical characterization were given elsewhere [10,17].

### 2.2. Ni/YSZ microstructure characterization

Ni/YSZ microstructure characterization was performed using scanning electron microscopy (SEM) equipped with energy dispersive spectroscopy (EDS) and electron backscatter diffraction (EBSD) detectors. X-ray mapping was used to show elemental distributions and new phase formation. EDS provided information on composition of new phases and the depth of interaction. EBSD confirmed specific crystal structures of alteration products.

## 3. Experimental results

When Ni/YSZ was exposed to 0.5–10 ppm $PH_3$ at 700–800 °C, nickel in the Ni–YSZ support was partially or completely converted to different Ni–P phases, depending on the exposure time and $PH_3$ concentration. Fig. 1 shows typical SEM image obtained from the anode-supported cell after test in synthetic coal gas with 2 ppm $PH_3$ at 750 °C. Appearance of the Ni–YSZ is seen to be dramatically altered compared to the initial microstructure. A sharp border between converted and unconverted Ni–YSZ is clearly seen in the middle of the image. Ni in the upper part of the anode support was fully converted into a mixture of different nickel phosphides, $Ni_3P$, $Ni_5P_2$, and $Ni_{12}P_5$. These crystals are seen to be much larger than unconverted Ni in Ni–YSZ in the lower part of the support, because of the associated coalescence and agglomeration [10]. The active anode near the YSZ electrolyte did not appear to be structurally affected. Large $Ni_2P$ and $Ni_{12}P_5$ crystals were formed on the anode surface, mostly because of nickel being drawn up out of the Ni/YSZ support by phosphorus.

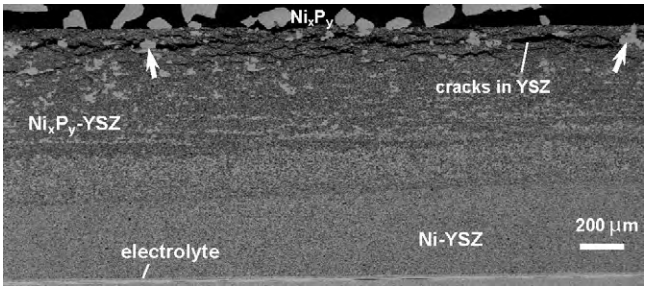


**Fig. 1.** Cross-sectional SEM image of the Ni–YSZ anode-supported button cell after 1700-h test in synthetic coal gas with 2 ppm $PH_3$ at 750 °C. Dense YSZ electrolyte is seen at the bottom of the image. Unaltered Ni–YSZ was found in the low part of the support and altered Ni–P–YSZ in the upper part of the support. All Ni-containing phases are light grey, YSZ is dark grey, pores and cracks are black. Arrows point at the large Ni–P agglomerates formed in the YSZ matrix in the upper part of the support causing stresses.

**Table 1**
Expected volume change from Ni conversion to nickel phosphide, $Ni_xP_y$.

| | Formula weight (FW) (g mol$^{-1}$) | Density (g cm$^{-3}$) | Volume change | Length ratio change |
|---|---|---|---|---|
| Ni | 58.7 | 8.902 [17] | 1 | 1 |
| $Ni_3P$ | 207.1 | 7.86 [17] | 1.332 | 1.099 |
| $Ni_5P_2$ | 355.5 | 7.71 [17] | 1.398 | 1.117 |
| $Ni_{12}P_5$ | 859.1 | 7.53 [18] | 1.442 | 1.128 |
| $Ni_2P$ | 148.4 | 7.35 [18] | 1.531 | 1.151 |

With the conversion of Ni to Ni–P, the volume of the Ni-containing phase changed. Calculations of the corresponding volume change to $Ni_3P$, $Ni_5P_2$, and $Ni_2P$ are given in Table 1. The volume change was different for the series of binary nickel phosphides, $Ni_2P$, $Ni_3P$, $Ni_5P_2$, to $Ni_{12}P_5$. The conversion from Ni phase to $Ni_2P$ phase appears to cause the largest volume expansion. Nickel phosphide agglomerates inside the anode support were seen to form stratified layers, Figs. 1 and 2. A layer of Ni-containing phase lying in parallel to the anode surface alternated with a contiguous layer that was virtually Ni-free. Stratification is expected to cause substantial internal stresses in the YSZ matrix, especially in the upper part of the support. It is apparent that stress development could not be accommodated by the available porosity in the YSZ matrix. Horizontal elongated cracks were developed in the nickel-free YSZ layer resulting in the anode support deformation, Fig. 1. Arrows point at the large Ni–P agglomerates inside the YSZ matrix that clearly initiated cracks.

## 4. Modeling and analysis

In this section the stress induced by the volume expansion during conversion from nickel to nickel phosphide was studied using finite element (FE) stress analysis.

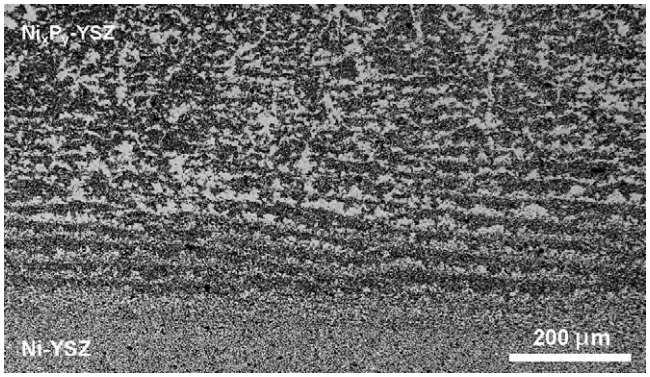


**Fig. 2.** Cross-sectional image of the anode support after 650-h test in synthetic coal gas with 1 ppm $PH_3$ at 800 °C. Unaltered fine Ni crystallites are at the bottom of the image and altered large $Ni_xP_y$ agglomerates are distinguished from the middle and up. Ni-containing phases are shown as light grey, YSZ is dark grey, and pores are black.

### 4.1. Meshing of microstructure-based stress analyses model

The Ni–YSZ microstructure shown in Fig. 3 was assumed as the representative volume element (RVE) and used in the subsequent finite element analysis. The area fractions of nickel, zirconia and pores within the structure were determined from the mixed elemental maps and analyzed using ImageJ software. In meshing the anode microstructure, the image was automatically segmented into two different phases using a photo-processing software such as Photoshop or Paint Shop Pro. The segmentation was done by adjusting colors such that all nickel grains ended up red while all YSZ grains ended up blue. Lines defining the boundaries between the two phases were then generated with the same software. The boundary-line image was imported next into ArcMap (a GIS software package) and converted from raster to vector form. The vectorized lines were then imported to Gridgen, a grid generating software package, to generate the 2D mesh with triangular elements. Each domain was then assigned a material and all the domains for a material were exported into a STL (a standard triangular mesh format) file which was used to export the data into MSC.MARC [19] format with nodes listed in counterclockwise fashion. Following the above image processing procedures, the finite element discretization for the microstructure shown in Fig. 3a was generated see Fig. 3b. In this model, only two initial phases were considered to be present in addition to the voids and perfect bonding was assumed between the two phases.

### 4.2. Material properties, loading and boundary conditions

The RVE illustrated in Fig. 3 was assumed to represent the cross-section of the Ni–YSZ anode. 2D plane strain element was used since the in-plane dimension of the cell was much larger than the thickness of Ni–YSZ anode. In this model, 31,700 plane strain linear triangular elements were used with 17,446 nodes. Both left and right sides of the microstructure-based model shown in Fig. 3b were constrained along the horizontal direction, and the vertical displacement was allowed. The bottom side was constrained of vertical displacement while allowing horizontal displacement. The topside of the model was treated as free surface. The volume expansion induced by the Ni phase conversion to the nickel phosphide was simulated by an isotropic straining model. This model was implemented into commercial finite element software MSC.MARC by user subroutine.

The temperature-dependent mechanical properties of pure Ni and YSZ phases were used in the stress analysis. Fig. 4 gives the Young's moduli of Ni and YSZ as a function of temperature [20,21].

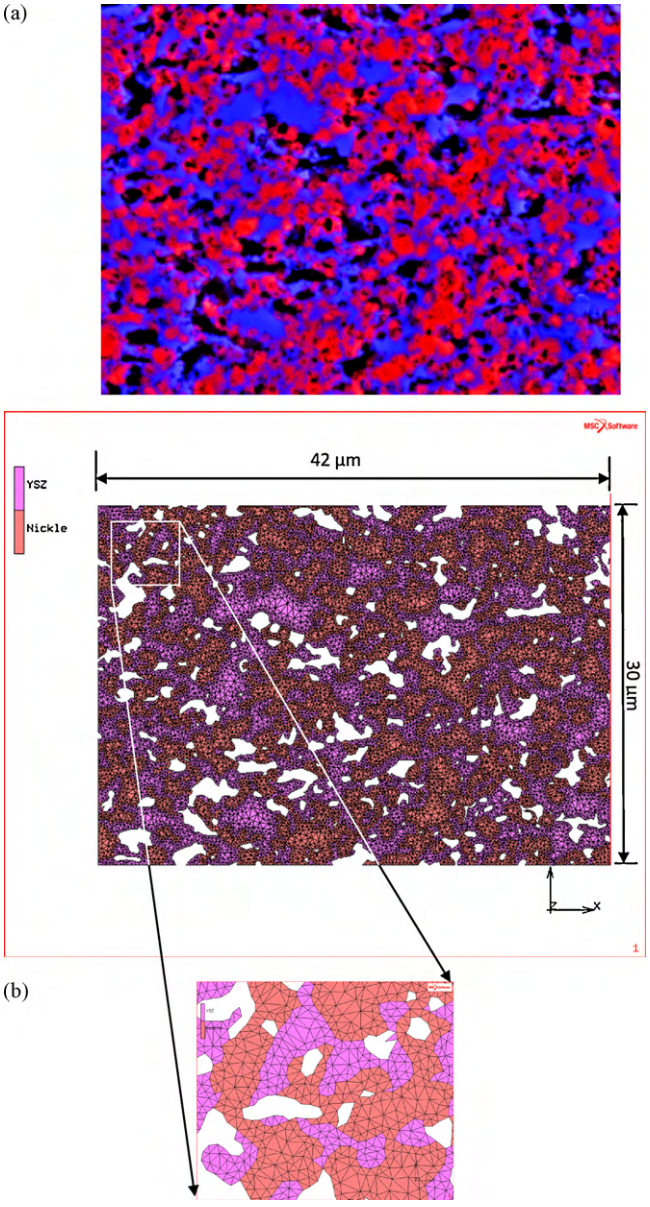


**Fig. 3.** (a) Ni/YSZ microstructure and distribution of two phases identified by Gatan Images. Nickel is red and YSZ is blue. (b) Finite element model used in analysis.

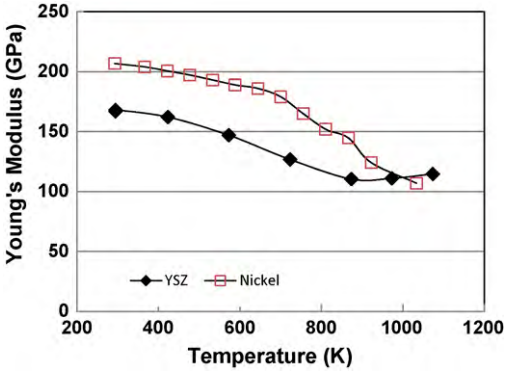


**Fig. 4.** Young's moduli of YSZ and Ni as a function of temperature.

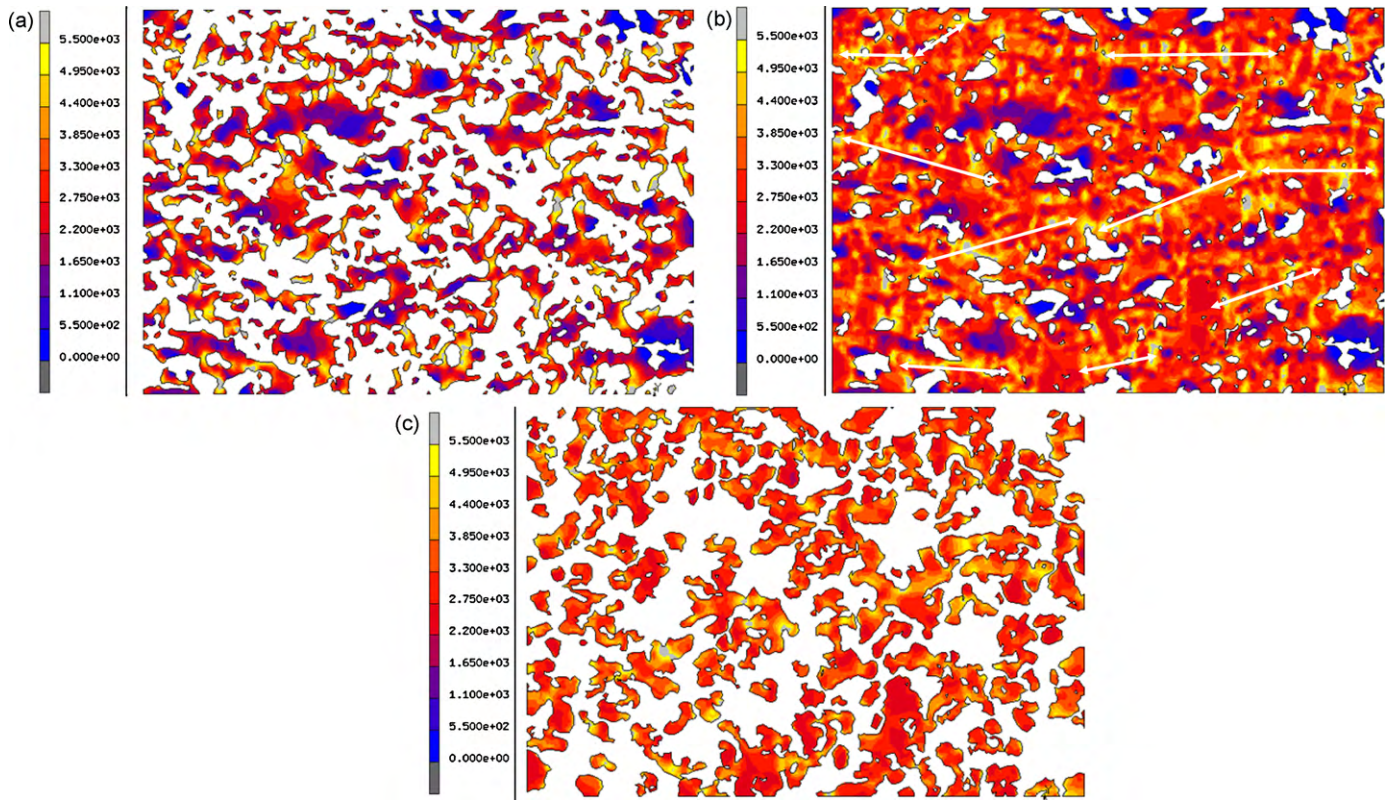


**Fig. 5.** (a) Distribution of von Mises stress (in MPa) in YSZ phase of the Ni–YSZ support induced by volume change due to Ni conversion to $Ni_2P$. (b) Evolution of equivalent von Mises stress (in MPa) of the Ni–YSZ support induced by volume change due to Ni conversion to $Ni_2P$. (c) Distribution of von Mises stress (in MPa) in Ni phase of Ni–YSZ anode induced by volume change due to Ni conversion to $Ni_2P$.

A constant and uniform temperature field was imposed on the RVE in Fig. 3; therefore no thermal stresses will be generated by the coefficient of thermal expansion (CTE) mismatch and temperature gradient. Only the volume expansion upon Ni conversion to a new phase was considered in the stress analysis to predict the stress distributions in the different phases. As given in Table 1, the conversion of Ni to $Ni_2P$ led to the largest volume expansion in comparison with $Ni_3P$, $Ni_5P_2$, and $Ni_{12}P_5$. Because of that, in the following analysis all altered nickel was assumed to be $Ni_2P$, with the modulus of 130 GPa [22].

### 4.3. Predicted stresses in Ni–YSZ support

In general, the depth of the nickel phosphide phase penetration into the Ni–YSZ support was non-uniform due to the strong Ni–P interactions and a mix of different Ni–P phases were found to coexist [10]. In this section, all the Ni crystallites in the RVE were assumed to be fully converted to $Ni_2P$. No partial conversion cases were considered.

Fig. 5 shows the distribution of equivalent von Mises stress in the YSZ phase, Ni–YSZ combined and Ni phase only, respectively. Fig. 5a depicts the distribution of equivalent von Mises stress only in the YSZ: many 'hot' spots with high localized stress were predicted. The highest stress level in the YSZ was predicted to be near 5 GPa, much higher than the strength of the YSZ tested at the operating temperature [20,23]. Therefore, localized failure in the form of localized micro-cracks is likely to appear first in the YSZ phase, and the cracks would subsequently propagate through the rest of the support, leading to the macro-cracks in the Ni–YSZ, see Fig. 5b. White arrows in Fig. 5b indicate the directions of potential propagation of the micro-cracks to form macro-cracks. These findings confirm that Ni volume expansion due to the transition from Ni to nickel phosphide is responsible for stress striation in the Ni–YSZ support. These high stress zones may result in transverse crack propagation.

Fig. 5c illustrates how many 'hot' spots (high stress level) were developed in the Ni–P phase, also with a very high magnitude, ~5 GPa. This is due to the fact that $Ni_2P$ was treated as elastic material. The melting point of $Ni_2P$ is near 870–890 °C [24], and because all of the tests were performed at 700–800 °C, Ni–P phase was at temperatures very close to melting. Therefore, considerable degree of softening and creep is expected to occur for $Ni_2P$ at operating temperatures, which should result in extensive grain growth and coalescence under a small amount of stress. These effects were not considered in the present study. Also, no stress assisted Ni–P conglomeration due to creep deformation is considered in the current study, and Ni coalescence and agglomeration is considered to be solely due to the high mobility of Ni–P phase at the operating temperatures. Any consideration of a stress assisted creep deformation at temperature will only exacerbate the above described anode structural degradation.

### 4.4. Predicted stresses in Ni–YSZ with varied fraction of Ni–P phase

In this section, the transformation of Ni to Ni–P phase was assumed to occur within certain distance from the anode surface toward the electrolyte at a given percentage. As shown in Fig. 6, 33%, 66%, and 100% of the total Ni–YSZ thickness, respectively, were considered to be affected by phosphorous, i.e., Ni particles within 1/3, 2/3 from the surface, or the whole Ni–YSZ support including the active anode were fully converted to Ni–P. Again, $Ni_2P$ was assumed to be the only nickel phosphide phase.

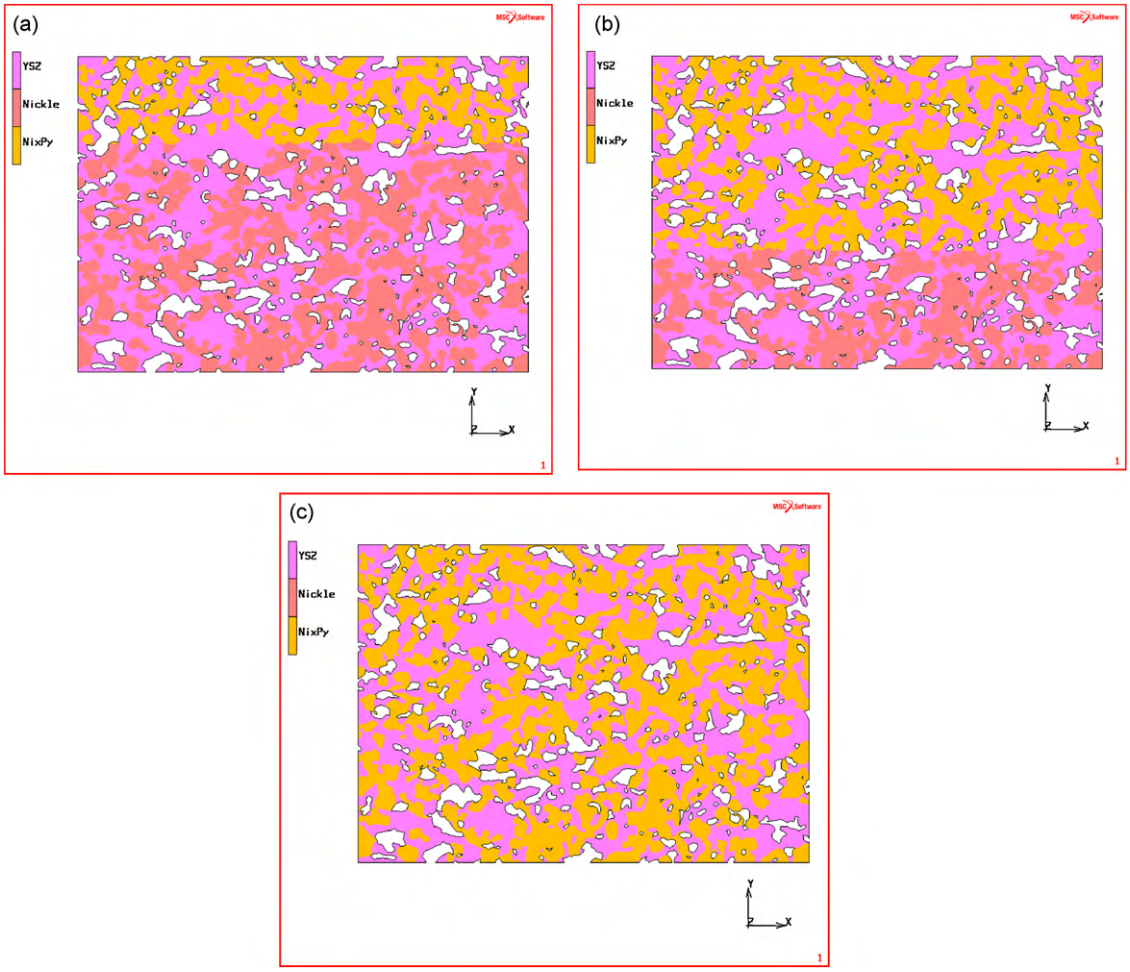


**Fig. 6.** of the Ni–YSZ support thickness where Ni was converted to Ni–P: (a) 33%; (b) 66%; (c) 100%.

Fig. 7 shows the equivalent von Mises stress in the Ni–YSZ support with varied phosphorus penetration depths. It can be seen that independent of the phosphorus penetration, the regions of very high stress were always predicted within the transformed zone. The nickel phosphide appears to act as a localized stress riser due to volume expansion. It is obvious that the stratified microstructure with horizontal alternating layers of Ni–P and YSZ given in Figs. 1 and 2 was a consequence of stress. The horizontal stripes were origins of the potential cracks. Compared to the reported strength of YSZ at operating temperatures [20,23], the stress induced by phosphorous was high enough to initiate the micro-cracks in the YSZ. The horizontal propagation of the micro-cracks would then form near-horizontal crack stripes in the anode support. Again, several main high stress stripes were predicted within the contaminated region, and no driving force was predicted for the cracks to spread out of the contaminated region. Such a localized degradation phenomenon indicates that only the structural integrity of the affected region will be compromised by the presence of phosphorus. Unaltered Ni–YSZ should not show any signs of structural degradation.

Indeed, as seen in Fig. 1, only the upper part of the Ni–YSZ support which was the closest to the fuel flow was affected the most. Because of the strong nickel–phosphorus interactions, Ni in that part was converted to a phosphorus-rich phase, $Ni_2P$. Further away from the fuel inlet or deeper inside the support in the electrolyte direction, when more unreacted Ni became available, lower phosphorus-containing phases, $Ni_{12}P_5$, $Ni_5P_2$ and $Ni_3P$, were detected by EDS and EBSD. The volume change induced by the Ni conversion to $Ni_5P_2$ is lower than that due to the $Ni_2P$ formations, see Table 1. Therefore, the stress level in the area where $Ni_2P$ was formed (i.e., the anode surface and area in the vicinity of surface) was the highest and resulted in initiation and propagation of several macroscopic lateral cracks. As seen in Fig. 1, the area further away from the surface had no cracks: Ni in that area was converted to $Ni_5P_2$ and $Ni_3P$ and the predicted volume changes were not as dramatic as those for $Ni_2P$ and the porous YSZ matrix was able to accommodate for such stress. Nickel at the active anode/electrolyte interface was not altered for the test duration and no microstructural changes in that area were observed. This is in agreement with Fig. 7, predicting no micro-crack formation or crack spreading into the unaffected area by phosphorus.

The above findings clearly indicate that it is necessary to establish tolerance limits for strongly interacting impurities in order to prevent SOFC from catastrophic failures due to the loss of structural integrity of the anode support for the expected lifetime of a stack.

## 5. Summary and conclusions

Effect of the phosphorus impurity in the synthetic coal gas on the mechanical degradation of the porous Ni–YSZ support was studied using a combined experimental/modeling approach. Phosphorus was chosen as an example of impurity exhibiting strong interactions with the Ni. The following conclusions can be summarized.

Phase conversion from Ni to Ni phosphide was found to result in large localized volume increase. The volume change was dependent on the nickel phosphide phase, and $Ni_2P$ caused the highest volume change in comparison with $Ni_3P$ and $Ni_5P_2$. Volume changes

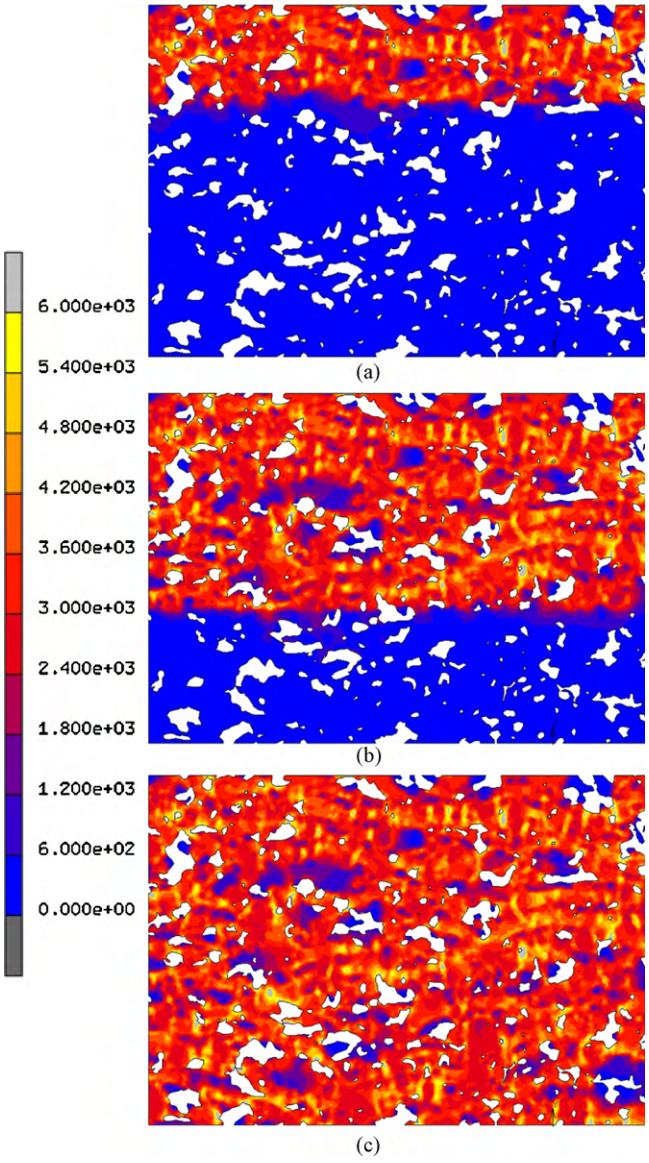


**Fig. 7.** Effect of phosphorus penetration into Ni–YSZ support on stress distribution: (a) 1/3 of the support; (b) 2/3 of the support; (c) fully converted support.

created high level of localized stresses in the Ni–YSZ anode support and led to the formation of localized micro-cracks and further crack coalescence in forming macroscopic cracks. The stress level was closely related to the conversion ratio of Ni phase to nickel phosphide. The high stress induced by the Ni phase conversion to a series of binary nickel phosphide phase is localized within the contaminated region, and will not create enough driving force for the cracks to propagate outside of the contaminated region.

To this end, determination of tolerance limits for strongly interacting impurities would not only inhibit the SOFC stack electrochemical performance degradation, it should also prevent SOFC from catastrophic failures due to the loss of structural integrity of the anode support for the expected lifetime of a stack.

## Acknowledgements

We would like to acknowledge Dr. D.J. Edwards and A. Schemer-Kohrn for performing SEM and EBSD analyses and fruitful discussions. The work was funded as part of the Solid-State Energy Conversion Alliance (SECA) Core Technology Program and Coal-Based Systems Core Research Program by the U.S. Department of Energy's National Energy Technology Laboratory (NETL). The Pacific Northwest National Laboratory is operated by Battelle Memorial Institute for the United States Department of Energy under Contract DE-AC06-76RL01830.

## References

[1] A. Boudghene Stambouli, E. Traversa, Renewable & Sustainable Energy Reviews 6 (2002) 433–455.
[2] W.P. Teagan, J.H.J.S. Thijssen, E.J. Carlson, C.J. Read, in: A.J. McEvoy (Ed.), Proceedings of the 4th European Solid Oxide Fuel Cell Forum, Lucerne, Switzerland, 2000, pp. 969–980.
[3] FutureGen: Integrated Hydrogen, Electric Power Production and Carbon Sequestration Research Initiative, U.S. Dept. of Energy Office of Fossil Energy, March 2004.
[4] M. Diaz-Somoano, M.R. Martinez-Tarazona, Fuel 82 (2) (2003) 137–145.
[5] M. Díaz-Somoano, M.E. Kylander, M.A. López-Antón, I. Suárez-Ruiz, M.R. Martínez-Tarazona, M. Ferrat, B. Kober, D.J. Weiss, Environmental Science and Technology 43 (4) (2009) 1078–1085.
[6] J.P. Trembly, R.S. Gemmen, D.J. Bayless, Journal of Power Sources 163 (2) (2007) 986–996.
[7] F.N. Cayan, M. Zhi, S.R. Pakalapati, I. Celik, N. Wu, R. Gemmen, Journal of Power Sources 185 (2) (2008) 595–602.
[8] O.A. Marina, L.R. Pederson, C.A. Coyle, E.C. Thomsen, G.W. Coffey, Transactions of the Electrochemical Society 25 (2) (2009) 2125–2130.
[9] C.A. Coyle, O.A. Marina, E.C. Thomsen, D.J. Edwards, C.N. Cramer, G.W. Coffey, L.R. Pederson, Journal of Power Sources 193 (2) (2009) 730–738.
[10] O.A. Marina, C.A. Coyle, E.C. Thomsen, D.J. Edwards, G.W. Coffey, L.R. Pederson, Solid-State Ionics 181 (8–10) (2010) 430–440.
[11] M. Zhi, X. Chen, H. Finklea, I. Celik, N.Q. Wu, Journal of Power Sources 183 (2) (2008) 485–490.
[12] W. Li, K. Hasinska, M. Seabaugh, S. Swartz, J. Lannutti, Journal of Power Sources 138 (1–2) (2004) 145–155.
[13] W.N. Liu, X. Sun, M.A. Khaleel, J.M. Qu, Journal of Power Sources 192 (2) (2009) 486–493.
[14] P. Kofstad, Materials Science & Engineering A: Structural Materials: Properties, Microstructure and Processing A120–121 (1989) 25–29.
[15] A.M. Huntz, Materials Science and Technology 4 (12) (1988) 1079–1088.
[16] A.M. Huntz, Materials Science & Engineering A: Structural Materials: Properties, Microstructure and Processing A201 (1–2) (1995) 211–228.
[17] D.R. Lide, Handbook of Chemistry and Physics, 80th Edition, CRC Press, 1999–2000.
[18] M.V. Landau, M. Herskowitz, T. Hoffman, D. Fuks, E. Liverts, D. Vingurt, N. Froumin, Industrial and Engineering Chemistry Research 48 (11) (2009) 5239–5249.
[19] MARC, 2007. Version 2007r1. http://www.mscsoftware.com/products/marc.cfm?Q=131&Z=396&Y=400.
[20] http://www.seca.doe.gov/~secamat.
[21] Nickel 201, Alloy Digest, Engineering Alloys Digest, Inc., Upper Montelair, NJ, 1969.
[22] X.D. Li, B. Bhushan, K. Takashima, C.K. Baek, Y.K. Kim, Ultramicroscopy 97 (2003) 481–494.
[23] M. Mori, Y. Hiei, H. Itoh, G.A. Tompsett, N.M. Sammes, Solid State Ionics 160 (2003) 1–14.
[24] C. Schmetterer, J. Vizdal, H. Ipser, Intermetallics 17 (2009) 826–834.